pharmaceutics

MDPI

Article

Gold Nanoclusters-Based NIR-II Photosensitizers with Catalase-like Activity for Boosted Photodynamic Therapy

Qing Dan [1,2], Zhen Yuan [3], Si Zheng [1,2], Huanrong Ma [1], Wanxian Luo [1], Li Zhang [1], Ning Su [1], Dehong Hu [2], Zonghai Sheng [2,*] and Yingjia Li [1,*]

[1] Department of Medicine Ultrasonics, Nanfang Hospital, Southern Medical University, Guangzhou 510515, China
[2] Shenzhen Institute of Advanced Technology, Chinese Academy of Sciences, Shenzhen 518055, China
[3] Faculty of Health Sciences, University of Macau, Taipa, Macau SAR, China
* Correspondence: zh.sheng@siat.ac.cn (Z.S.); lyjia@smu.edu.cn (Y.L.)

Abstract: Photodynamic therapy (PDT) under fluorescence imaging as a selective and non-invasive treatment approach has been widely applied for the therapy of cancer and bacterial infections. However, its treatment efficiency is hampered by high background fluorescence in the first near-infrared window (NIR-I, 700–900 nm) and oxygen-dependent photosensitizing activity of traditional photosensitizers. In this work, we employ gold nanoclusters (BSA@Au) with the second near-infrared (NIR-II, 1000–1700 nm) fluorescence and catalase-like activity as alternative photosensitizers to realize highly efficient PDT. The bright NIR-II fluorescence of BSA@Au enables the visualization of PDT for tumor with a high signal-to-background ratio (SBR = 7.3) in 4T1 tumor-bearing mouse models. Furthermore, the catalase-like activity of BSA@Au endows its oxygen self-supplied capability, contributing to a five-fold increase in the survival period of tumor-bearing mice receiving boosted PDT treatment compared to that of the control group. Moreover, we further demonstrate that BSA@Au-based PDT strategy can be applied to treat bacterial infections. Our studies show the great potential of NIR-II BSA@Au as a novel photosensitizer for boosted PDT against cancer and bacterial infections.

Keywords: photodynamic therapy; NIR-II fluorescence; gold nanoclusters; hypoxia; nanozyme; cancer theranostics

Citation: Dan, Q.; Yuan, Z.; Zheng, S.; Ma, H.; Luo, W.; Zhang, L.; Su, N.; Hu, D.; Sheng, Z.; Li, Y. Gold Nanoclusters-Based NIR-II Photosensitizers with Catalase-like Activity for Boosted Photodynamic Therapy. *Pharmaceutics* **2022**, *14*, 1645. https://doi.org/10.3390/pharmaceutics14081645

Academic Editors: Manivasagan Panchanathan and Eue-Soon Jang

Received: 22 June 2022
Accepted: 3 August 2022
Published: 7 August 2022

1. Introduction

Photodynamic therapy (PDT) is acknowledged as a clinical treatment modality for cancer and bacterial infections, which is selective, non-invasive, and feasible to combine with imaging. It generally employs a visible or near-infrared laser to excite photosensitizers to generate fluorescence (FL) for guiding therapy. Meanwhile, it generates singlet oxygen ($^1O_2$) in the presence of oxygen to kill cancer cells and bacteria [1–4]. To date, organic dyes (i.e., porphyrins, indocyanine dyes, BODIPYs, and aggregation-induced emission dyes) [5–8], inorganic nanoparticles (i.e., quantum dots, black phosphorus, and TiO_2) [9–11], polymer nanoparticles (i.e., polyfluorene and polythiophene) [12,13], and other nanomaterials (i.e., noble metal complexes and metallic nanomaterials) [14,15], have been developed for PDT. However, the FL emission of these photosensitizers is limited in visible (400–700 nm) and the first near-infrared (NIR-I, 700–900 nm) windows, resulting in intravital imaging with high background signal. Moreover, the $^1O_2$ generation of photosensitizers gradually decreases within tissue due to the pre-existing hypoxia and consumption of oxygen during the PDT process, leading to unsatisfactory PDT outcomes [16]. Therefore, it is of great significance to develop novel photosensitizers with long emission wavelength and self-supplied oxygen for boosted PDT against tumors and infectious diseases.

In recent years, several dyes with photosensitive activity in the second near-infrared (NIR-II, 1000–1700 nm) window have been explored, which exhibits unique merits over the

NIR-I window, such as a reduction in photon absorption and scattering, as well as improvement of signal-to-background ratio (SBR) [17–19]. However, these NIR-II photosensitizers generally show low PDT efficiency due to the oxygen insufficiency within laser irradiation area. Recently, NIR-II gold nanoclusters (NCs), consisting of several to about a hundred gold atoms with a size below 3 nm, are of particular interest to researchers owing to their intrinsic FL emission, renal clearance, and high biocompatibility [20]. Gold NCs with the NIR-II emission have been developed for the bright in vivo NIR-II FL imaging of malignant tumors, bones, and brain vessels [21–25]. In addition to FL imaging capability, gold NCs could also generate toxic $^1O_2$ under NIR laser irradiation [26]. Furthermore, our previous studies reported that gold NCs showed catalase-like activity, which could decompose endogenous hydrogen peroxide (H_2O_2) within tumor tissue to O_2 for enhancing PDT [27]. However, to our best knowledge, there has no reports on the utilization of the three features of gold NCs, including NIR-II FL, $^1O_2$ generation, and catalase-like activity, for boosted PDT against tumors and bacterial infections.

Herein, we developed the NIR-II gold NCs (BSA@Au) as novel photosensitizers for boosted PDT. As shown in Scheme 1, BSA@Au was synthesized by one-step biomineralization. The facile synthesis process is advantageous for biological applications. The bright NIR-II FL of BSA@Au could realize high-performance in vivo bioimaging for the optimization of PDT. Meanwhile, the superb catalase-like activity of BSA@Au could catalyze the decomposition of excess H_2O_2 to produce O_2 within the microenvironment of the tumor and bacterial-infected tissues for enhancing PDT. Our studies provide a paradigm of using gold NCs as efficient photosensitizers for boosted PDT.

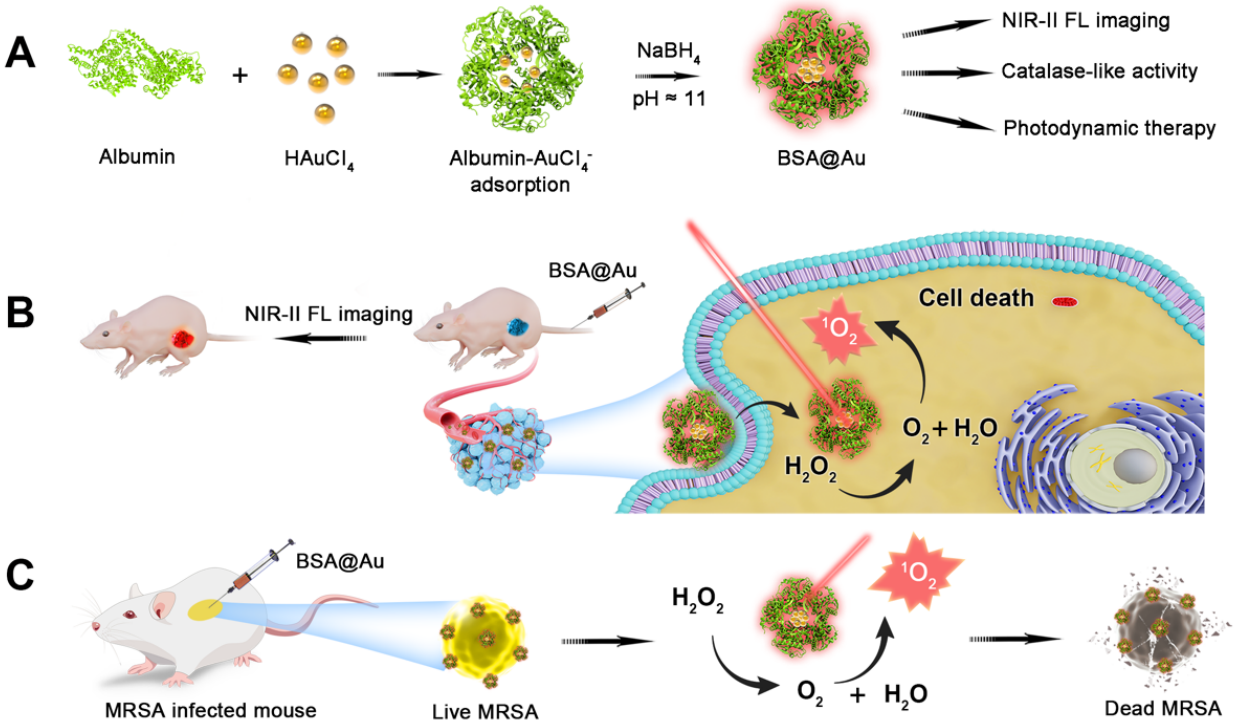

Scheme 1. Scheme of NIR-II BSA@Au enhancing PDT. (**A**) Synthesis of NIR-II BSA@Au. (**B**) BSA@Au combining with PDT against breast cancer. (**C**) BSA@Au combining with PDT against methicillin-resistant *Staphylococcus aureus* (MRSA) infection.

2. Materials and Methods

2.1. Materials

Gold (III) chloride trihydrate ($HAuCl_4 \cdot 3H_2O$), bovine serum albumin (BSA), sodium borohydride ($NaBH_4$), and 1,3-Diphenylisobenzofuran (DPBF) were provided by Sigma-

Aldrich. The Cell counting kit-8 (CCK-8) was supplied by Dojindo. Pimonidazole HCl and IgG_1 mouse antibody (conjugated with FITC) were purchased from Hypoxyprobe.

2.2. Synthesis of BSA@Au

BSA@Au was prepared adapted from previous reports [28]. Briefly, all glassware were soaked with aqua regia (HCl:HNO_3, volume ratio 1:3), then washed with ultrapure water. $HAuCl_4$ solution (10 mM, 1.25 mL) was mixed with BSA solution (0.76 mM, 2.5 mL). Then, NaOH solution (1 M, 0.25 mL) and $NaBH_4$ (0.1 M, 0.1 mL) were introduced. The whole process was under vigorously stirring. When the mixture turned into deep brown, it was incubated in a shaker (180 rpm, 37 °C) for 12 h to obtain BSA@Au nanoclusters. The as-prepared BSA@Au was purified by dialysis (molecular weight cutoff: 8–14 KD) with 0.1 M phosphate solution (pH ≈ 7.4) and stored in the dark at 4 °C for further investigation.

2.3. In Vivo FL Imaging

Mice bearing a 4T1 tumor received an intravenous (i.v.) injection of BSA@Au (0.46 mM, 200 μL) and were imaged at 0, 2, 4, 10, and 24 h. At 10 h, the main organs (including heart, liver, spleen, lung, and kidneys) and tumor were collected for ex vivo FL imaging. NIR-I FL imaging was conducted with excitation wavelength at 675 nm, and emission wavelength at 800 nm. The NIR-II FL imaging conditions were set as follows: excitation wavelength: 808 nm; long-pass filter: 1000 nm; and exposure time: 800 ms.

2.4. In Vivo PDT for Tumor

To evaluate the PDT efficacy, we randomly divided Balb/C mice bearing 4T1 tumor into 4 groups (n = 5): (1) Control; (2) Laser; (3) BSA@Au; (4) BSA@Au + Laser. At 10 h post i.v. injection of BSA@Au, the 808 nm laser (0.3 W/cm^2, 30 min) was applied and the temperature of tumors in group (4) was recorded to avoid the thermal effect. Since the single dose treatment, the tumor volumes and body weights of mice were recorded every 2 days for further analysis. When tumor grew to ~800 mm^3, the mouse was defined as dead to obtain the survival curve.

2.5. In Vitro Antibacterial Assay

For antibacterial experiments, the amounts of live MRSA after PDT treatment were quantified by plate counting method. Firstly, MRSA suspensions were mixed with PBS, BSA@Au, and H_2O_2 (200 μM). Then, the suspensions (OD_{600nm} ≈ 0.1) were placed in 96-well plates. After incubation at 37 °C for 30 min, the samples were further illuminated by 808 nm laser (0.3 W/cm^2, 30 min). Then, the suspensions were diluted (1:1 × 10^5) and transferred to LB agar plates for further cultivation at 37 °C. After 24 h, the colonies were counted by ImageJ software. In addition, bacterial morphology details of MRSA after different treatments were observed by scanning electron microscopy (SEM).

2.6. In Vivo PDT for MRSA Infection

To investigate in vivo antimicrobial performance, the infected mice were randomly divided into 4 groups (n = 5): (1) Control; (2) Laser; (3) BSA@Au; (4) BSA@Au + Laser. Mice of groups (3) and (4) were locally treated with BSA@Au solution (2.5 mM, 20 μL) at wound sites. The wound areas and body weights were recorded every 3 days. After 12 days of treatments, the wounds were excised for H&E staining analysis.

2.7. Statistical Analysis

Data are shown as the mean ± SD. Statistical significance was analyzed by student's *t*-test analysis. $p < 0.05$ was considered as statistical significance.

3. Results and Discussion

3.1. Preparation and Characterization of NIR-II BSA@Au

In this work, NIR-II emissive BSA@Au was synthesized by the biomineralization method. BSA was used as a template and protector for the growth of BSA@Au, and $NaBH_4$ was introduced as the critical reductant to modulate the NIR-II FL emission intensity. As shown in the high-resolution transmission electron microscope (HRTEM) image, the core size of BSA@Au was ~2 nm (Figure 1A), which was below the glomerular filtration cutoff (~6 nm) for renal clearance after i.v. injection [29,30]. The hydrodynamic diameter of BSA@Au was 10.1 ± 1.4 nm and stayed highly stable after four weeks of storage in water or fetal bovine serum (FBS) (Figure 1B,C). The size of BSA@Au measured by dynamic light scattering (DLS) was larger than that determined by HRTEM because DLS detected an average hydrodynamic size whereas the HRTEM images exhibited the dehydration morphology of BSA@Au [31].

Generally, gold-based nanoparticles exhibit FL emission in both NIR-I and NIR-II windows. We used the NIR FL spectrum instrument and NIR-II FL imaging system to verify the FL property of BSA@Au. When prepared under various conditions, it demonstrated different fluorescent performance. We noted that the NIR-II FL intensity of BSA@Au was closely related to the molar ratio of BSA: $HAuCl_4$ and NaOH: $NaBH_4$, which were optimized to be 0.15 and 25, respectively. Particularly, BSA@Au did not show NIR-II FL emission without $NaBH_4$ (Table S1, Figures 1D,E and S1A), which indicated the important reduction role of $NaBH_4$ to transfer Au^{3+} to Au to form the gold nucleus [32,33]. Furthermore, it was observed that NIR-II BSA@Au were formed rapidly within 0.5 h after adding $NaBH_4$, and the FL intensity gradually became stronger with the reaction time, reaching the peak value at 12 h, before decreasing (Figure S1B,C). Therefore, BSA (0.76 mM, 2.5 mL), $HAuCl_4$ (10 mM, 1.25 mL), NaOH (1 M, 0.25 mL), and $NaBH_4$ (0.1 M, 0.1 mL) were applied to synthesize NIR-II emissive BSA@Au under 37 °C for 12 h for further study.

To obtain deep insights into the optical properties of BSA@Au, its spectra properties were investigated. As shown in Figure 1F, the UV–Vis absorption spectrum of BSA@Au showed strong absorption at ~280 nm and decayed exponentially towards ~1100 nm. Moreover, the fluorescence emission spectrum exhibited two characteristic emission peaks at ~960 nm and ~1010 nm, reaching the NIR-II region. The mechanism of NIR-II emission of BSA@Au might involve complex electron transfer between BSA and gold cores [34]. In addition, we obtained the FL spectra of BSA@Au under various excitation wavelengths (450~808 nm). It showed an excitation wavelength-dependent FL emission peak, and the optimized FL emission spectrum was under 808 nm excitation (Figure S1D). Such a broadband-excitable bright FL emission was beneficial for diverse applications, and 808 nm excitation was chosen for further investigation.

Then, we used IR-26 as the reference and measured the fluorescent QY of the BSA@Au. Results showed that the QY of BSA@Au was measured to be ~3.5% (Figure S2), which was much higher than the QY of other NIR-II gold NCs (Table 1) and enabled it to realize bright FL imaging performance. Next, we tested the penetration depth of BSA@Au. Firstly, in the NIR-I window, the Eppendorf tube containing BSA@Au could not be detected when covered by chicken tissues (>4 mm thickness). In contrast, bright images of BSA@Au were obtained in NIR-II window at a penetration depth of more than 10 mm with high SBR (Figure S3A). This indicated the potential that BSA@Au could achieve high-performance in vivo imaging. Next, we assessed the photostability of BSA@Au compared with the clinical NIR dye indocyanine green (ICG). It was found that, under NIR-II FL imaging, BSA@Au was still bright under 808 nm laser irradiation (0.3 W/cm^2, 30 min) whereas the FL intensity of its ICG counterpart nearly decreased to ~0%, demonstrating that BSA@Au exhibited excellent photostability in contrast with ICG (Figure S4), which was owing to the role of BSA to protect BSA@Au from bleaching [35]. Taken together, the as-synthesized NIR-II emissive BSA@Au with a size of ~2 nm showed good water solubility, hydrodynamic size stability, photostability, and high QY of ~3.5%, demonstrating promising biomedical applications.

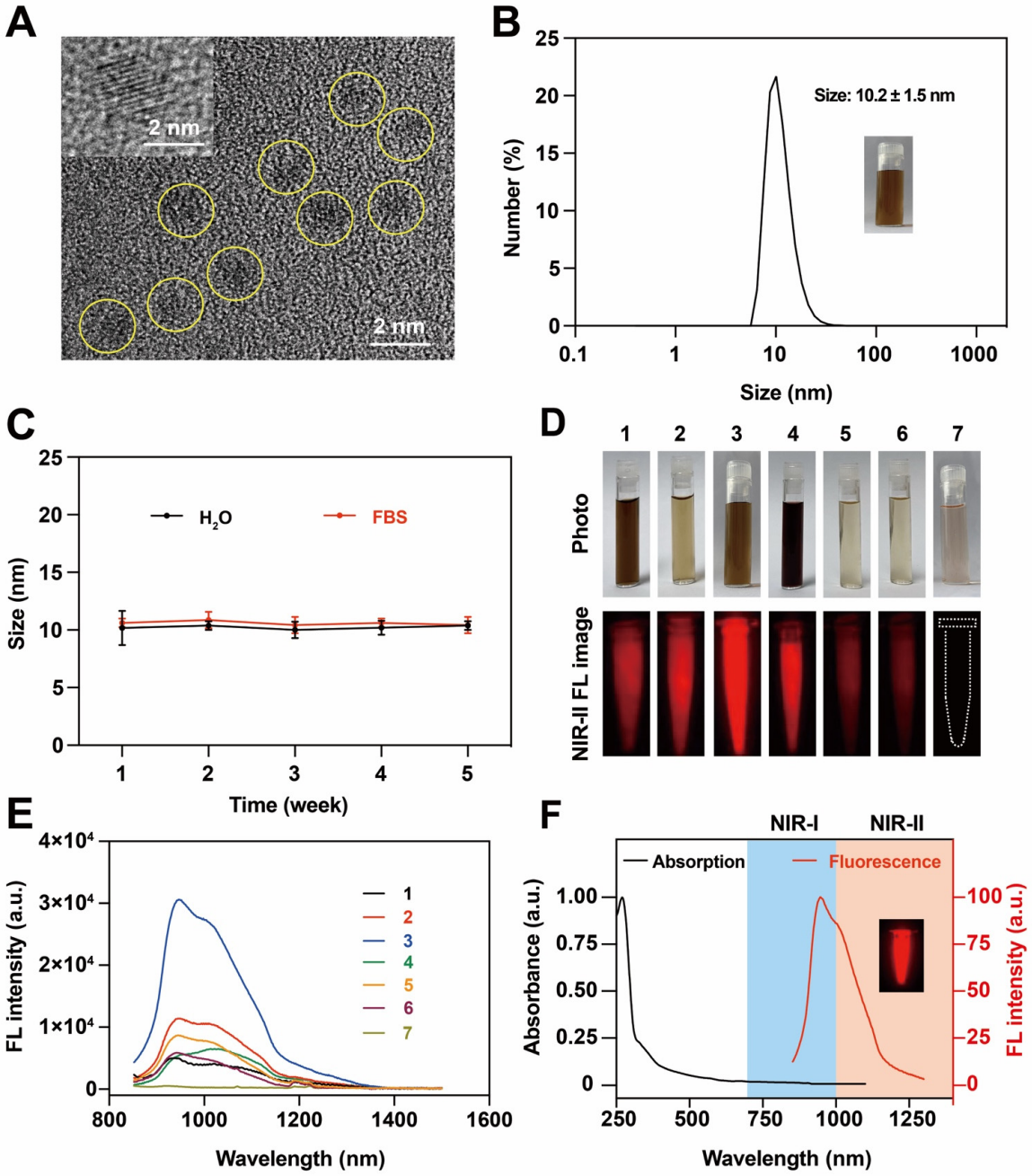

Figure 1. Characterization of BSA@Au. (**A**) The HRTEM image of BSA@Au. The inset was the lattice structure of BSA@Au. (**B**) Hydrodynamic size of BSA@Au. The inset was the digital photo of BSA@Au. (**C**) Colloidal stability of BSA@Au in H_2O or FBS after 4 weeks storage at 4 °C. (**D**) Digital photos and NIR-II FL images of BSA@Au samples 1–7 synthesized under different conditions. (**E**) The FL emission spectra of BSA@Au samples 1–7 under 808 nm excitation. In (**D**,**E**), 1: BSA@Au (50 mg/mL, 2.5 mL), $HAuCl_4$ (10 mM, 2.5 mL), NaOH (1 M, 0.25 mL), and $NaBH_4$ (0.1 M, 0.25 mL); 2: BSA@Au (50 mg/mL, 2.5 mL), $HAuCl_4$ (10 mM, 0.75 mL), NaOH (1 M, 0.25 mL), and $NaBH_4$ (0.1 M, 0.25 mL); 3: BSA@Au (50 mg/mL, 2.5 mL), $HAuCl_4$ (10 mM, 1.25 mL), NaOH (1 M, 0.25 mL), and $NaBH_4$ (0.1 M, 0.1 mL); 4: BSA@Au (50 mg/mL, 0.75 mL), $HAuCl_4$ (10 mM, 2.5 mL), NaOH (1 M, 0.25 mL), and $NaBH_4$ (0.1 M, 0.1 mL); 5: BSA@Au (50 mg/mL, 2.5 mL), $HAuCl_4$ (10 mM, 0.75 mL), NaOH (1 M, 0.5 mL), and $NaBH_4$ (0.1 M, 0.05 mL); 6: BSA@Au (50 mg/mL, 2.5 mL), $HAuCl_4$ (10 mM, 0.75 mL), NaOH (1 M, 1 mL), and $NaBH_4$ (0.1 M, 0.05 mL); 7: BSA@Au (50 mg/mL, 2.5 mL), $HAuCl_4$ (10 mM, 1.25 mL), and NaOH (1 M, 0.25 mL). (**F**) Absorption spectrum and FL spectrum of BSA@Au. The inset was the NIR-II FL image of BSA@Au.

Table 1. Overview of NIR-II emissive gold NCs.

Gold NCs	Core Size (nm)	QY (%)	Applications	Ref.
CD-Au NCs	1.85 ± 0.24	0.11	FL imaging of cancer	[21]
$Au_{25}(SG)_{18}$	3.2	0.67	FL imaging of brain injury and tumor metastasis	[22]
$Au_{25}(SG)_{18}$	3.30 ± 0.82	0.27	FL imaging of bones	[23]
$Au_{25}(SG)_{18}$-Pt	3.2	0.04	FL imaging guided chemotherapy	[24]
RNase-A@AuNCs	2.2 ± 0.1	1.19	FL imaging of gastrointestinal tract	[25]
$Au_{25}(SR_1)_x(SR_2)_{18-x}$	1.8	0.54	Antibacterial infections	[36]
Ln@AuNCs	35	/	In vivo FL imaging of H_2S	[37]
NR@Min-23@AuNCs	6.4	0.21	PDT theranostics against breast cancer	[38]
BSA@Au	2	3.53	Phototheranostics of cancer and bacterial infections	This work

3.2. Catalase-like Activity and Singlet Oxygen Generation

Tumor and infection microenvironments generally show high H_2O_2 concentration and low O_2 level [39,40]. We hypothesized that the as-prepared BSA@Au could serve as a catalase mimic to alleviate hypoxic microenvironment within tumor and infected tissues (Figure 2A). In a typical experiment, after BSA@Au was added into H_2O_2 solution, we observed obvious gas bubbles generated from the mixed solution (Figure 2B). Furthermore, when BSA@Au reacted with H_2O_2 monitored by an ultrasound imaging system, it showed significantly enhanced imaging performance both on B mode and contrast-enhanced ultrasound mode (Figure 2C). More interestingly, clear gas echo signals were observed in 4T1 tumor-bearing mice injected with BSA@Au under an ultrasound imaging system (Figure S5A), demonstrating that BSA@Au could catalyze H_2O_2 to produce O_2.

To gain deep understanding of the catalase-like activity of BSA@Au, we investigated the apparent kinetic parameters according to Michaelis-Menten method and Lineweaver-Burk equation [41]. We found that O_2 production was dependent on the concentration of BSA@Au and H_2O_2 (Figure 2D,E). Hence, it was believed that with more BSA@Au accumulation at the tumor sites or bacteria-infected lesions, more O_2 would generate in situ. In Figure S5B, the critical enzyme kinetic parameters of the Michaelis-Menten constant (K_m) and maximum initial velocity (V_{max}) were obtained and compared with other nanozymes. In this study, the apparent K_m reflected that BSA@Au showed high affinity towards H_2O_2, and V_{max} indicated the good catalytic ability of BSA@Au, which were superior to other nanozymes (Table S2). However, compared with our previous study, the V_{max} of BSA@Au was lower than that of Au NCs-ICG (with a size of ~1 nm) by an order of magnitude, which might be attributed to the relatively larger size and less turnover number of BSA@Au [27]. Moreover, in the future, the size, shape, and ligand effects should be considered to improve the catalytic performance of BSA@Au.

Next, we evaluated the $^1O_2$ generation ability of BSA@Au using 1,3-Diphenylisobenzofuran (DPBF) probe under 808 nm irradiation. Compared with the clinical photosensitizer ICG ($^1O_2$ generation efficiency, $\Phi_{\Delta ICG}$ = 0.2%), the $\Phi_{\Delta BSA@Au}$ was determined to be about 0.4% (Figure 2F), which was 2.2-fold higher than that of ICG. More inspiringly, our results showed that the generated O_2 from H_2O_2 degradation could enhance the generation of $^1O_2$, which could overcome the pre-existing hypoxia and O_2 depletion during the PDT process. In brief, upon 808 nm laser irradiation, the $^1O_2$ generation of BSA@Au was measured by DPBF. As shown in Figure 2G, the DPBF was quenched by BSA@Au combining with 808 nm laser irradiation, and significantly decreased after the addition of H_2O_2. This suggested that BSA@Au could serve as a self-sufficient O_2 supplying photosensitizer within H_2O_2-rich regions and thus enhance in vivo PDT for cancer and bacteria-infected diseases.

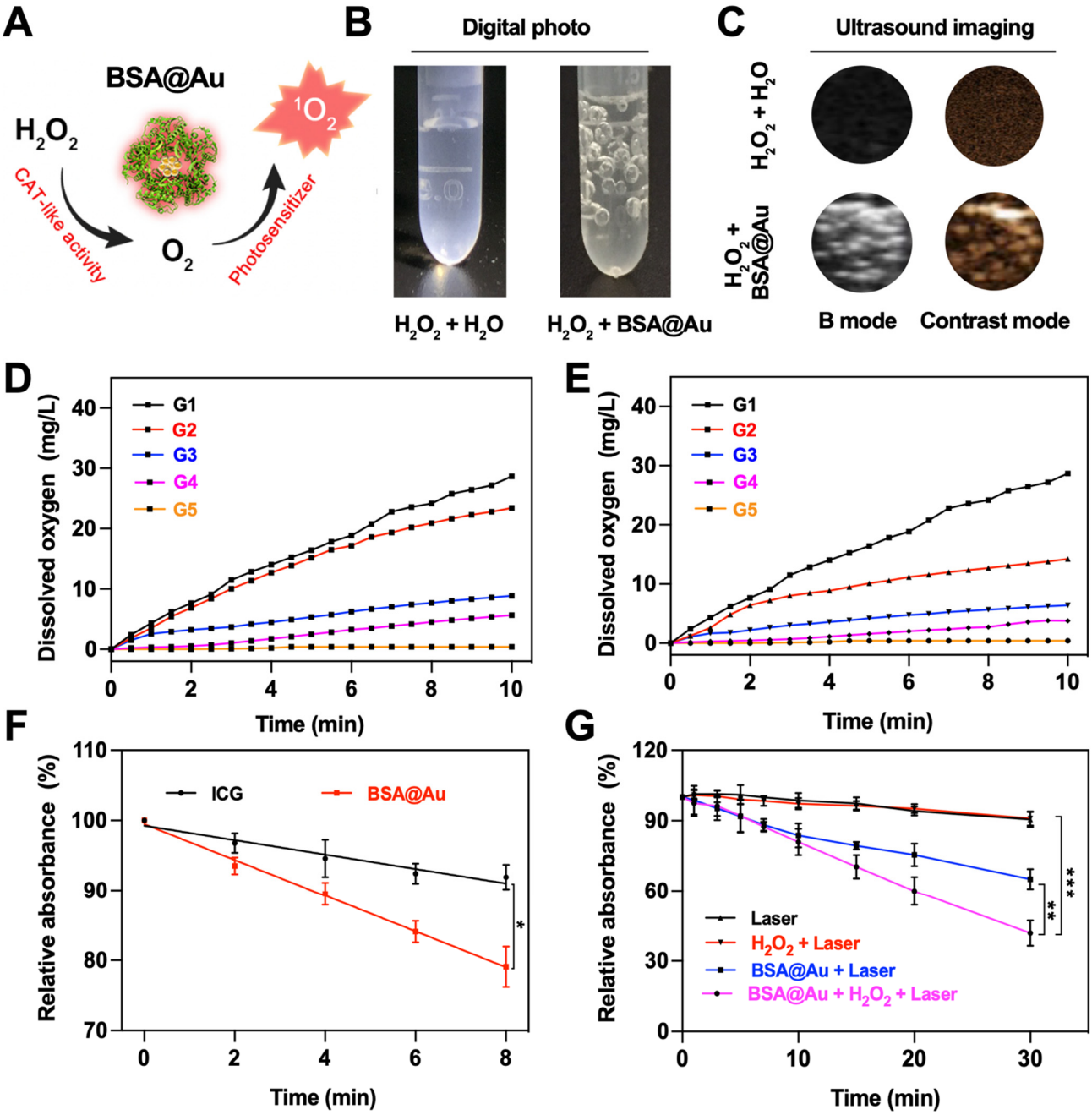

Figure 2. Catalase (CAT)-like activity and $^1O_2$ generation ability of BSA@Au. (**A**) Scheme of BSA@Au worked as a catalase mimic and photosensitizer in cascade reactions. (**B**) Photograph of bubbles generated from reaction between BSA@Au and H_2O_2. (**C**) Bubbles generation imaged by ultrasound device on B mode and contrast mode. (**D**) O_2 production from H_2O_2 of different concentrations decomposed by BSA@Au. G1: H_2O_2 (12.5 mM) + BSA@Au (0.23 mM); G2: H_2O_2 (9.37 mM) + BSA@Au (0.23 mM); G3: H_2O_2 (6.25 mM) + BSA@Au (0.23 mM); G4: H_2O_2 (1.25 mM) + BSA@Au (0.23 mM); G5: H_2O_2 (12.5 mM) + H_2O. (**E**) O_2 production from H_2O_2 catalyzed by BSA@Au of various concentrations. G1: H_2O_2 (12.5 mM) + BSA@Au (0.23 mM); G2: H_2O_2 (12.5 mM) + BSA@Au (0.12 mM); G3: H_2O_2 (12.5 mM) + BSA@Au (0.06 mM); G4: H_2O_2 (12.5 mM) + BSA@Au (0.03 mM); G5: H_2O_2 (12.5 mM) + H_2O. (**F**) $^1O_2$ production efficiency of BSA@Au measured by DPBF in absorbance at 414 nm under 808 nm laser irradiation with ICG as a reference. (**G**) $^1O_2$ generation measured by DPBF at 414 nm against time in the presence of different solutions. * $p < 0.5$, ** $p < 0.01$, *** $p < 0.005$.

3.3. Toxicity Evaluation and In Vitro PDT

The cytotoxicity of BSA@Au was investigated using the CCK-8 assay. The 4T1 cells were incubated with BSA@Au of various concentrations. Compared with the control groups, there was almost no obvious cell viability decrease in 4T1 cells treated with BSA@Au (Figure 3A), which indicated the low cytotoxicity of BSA@Au. Similarly, BSA@Au exhibited no harm to red blood cells in hemolysis assay (Figure 3B). Based on the above results, we confirmed the negligible in vivo toxicity of BSA@Au. Two weeks after i.v. injection of the BSA@Au with high concentration (5 mM, 100 μL), the blood samples and main organs, including heart, liver, spleen, lung, and kidneys, were collected from mice for blood routine examinations and H&E analysis, respectively. This showed that the tissue sections and blood indicators of BSA@Au group were not significantly altered compared to normal references (Figure S6, Table S3). The superior biocompatibilities of the BSA@Au might be attributed to the natural carrier of BSA and the ultrasmall size of BSA@Au, which together supported the in vivo application of BSA@Au for imaging and therapy.

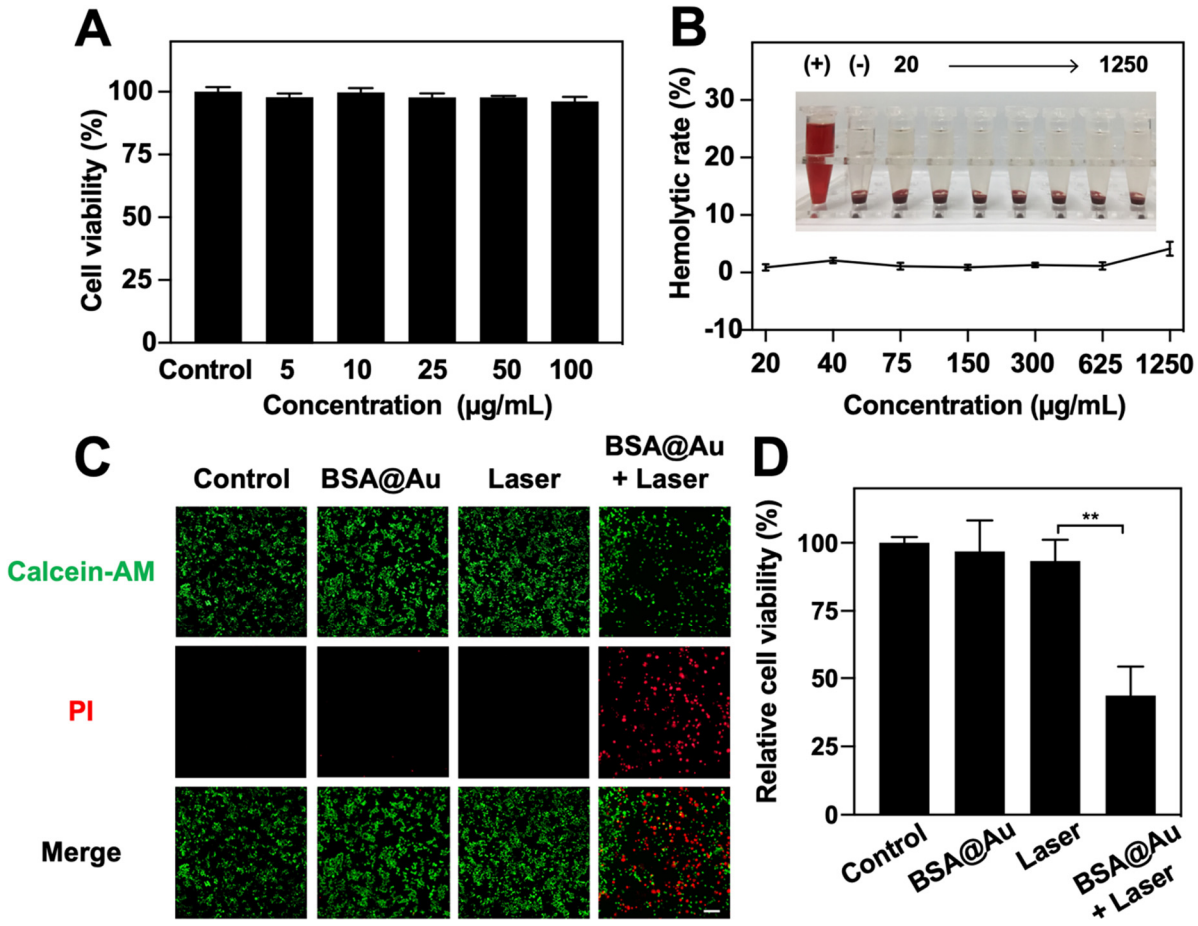

Figure 3. Cytotoxicity and in vitro anti-tumor PDT. (**A**) Cytotoxicity evaluation on 4T1 cells incubated with BSA@Au. (**B**) Hemolytic assay of BSA@Au on red blood cells (RBCs) from Balb/C mice. (+) represented RBCs solution mixed with ultrapure water; (−) indicated RBCs solution mixed with PBS. (**C**) Live/dead 4T1 cells visualization post PDT. The scale bar was 100 μm. (**D**) 4T1 cells viability post PDT. ** $p < 0.01$.

Given the high $^1O_2$ generation ability of BSA@Au, we tested the PDT efficacy against 4T1 cells. As shown in Figure 3C, Calcein-AM and PI dyes were used to visually evaluate the live/dead 4T1 cells after PDT. Nearly no red FL signals were detected in the control, BSA@Au, and Laser groups, while intense red FL signals in the BSA@Au + Laser group were observed. Cell viability after PDT was further quantified by CCK-8 method, revealing

that only ~43.7% cells survived when treated by BSA@Au and laser irradiation. However, control groups did not show obvious damage to 4T1 cells (Figure 3D). These results demonstrated the efficient PDT potential of BSA@Au.

3.4. In Vivo Imaging

Inspired by in vitro FL imaging performance of BSA@Au, the in vivo NIR-I and NIR-II FL imaging of BSA@Au was evaluated in 4T1 tumor-bearing mice. As illustrated in Figure 4A, images in the NIR-I window roughly outlined the tissue, due to the absorption and scattering of NIR-I photons by biological tissues. However, the imaging quality was well improved in the NIR-II window, showing the superiority of NIR-II FL imaging. Clearly, the FL signals of the tumor region were gradually increased with time and reached the accumulation peak at 10 h post-injection, and then gradually declined. The SBR was quantitatively analyzed. The tumor FL signal shows about 7.3-fold higher than that of background at 10 h post injection (Figure 4B), which could precisely discriminate and localize the tumor tissues. In addition, the metabolism and biodistribution of BSA@Au in major organs and tumor were investigated by ex vivo NIR-II FL imaging. As shown in Figures 4C and S7A, at 10 h post i.v. injection, the heart, lung, spleen, and kidneys exhibited nearly no or weak FL signals, while the liver and tumor showed strong FL intensity, suggesting the BSA@Au preferred to accumulate in these organs. The effective accumulation of BSA@Au in tumor could reduce the nanoparticles injection dosage to minimize the system hazards. Furthermore, different metabolic behaviors of BSA@Au in liver and kidneys were observed. The liver gradually exhibited FL signals within 10 h post injection of BSA@Au, while the kidneys showed bright FL signals at 0.5 h and 4 h post-injection, and the signal became weak at 10 h (Figure S7B,C). In addition, the signal of tumor and main organs (heart, liver, spleen, lung, and kidneys) remarkably decreased at 48 h post injection (Figure S7D,E). This suggested that BSA@Au could be cleared out from liver and kidneys because of the small size. Taken together, these important features enabled BSA@Au to be a promising medical probe for in vivo imaging to guide therapy.

3.5. In Vivo Anti-Tumor Therapy

Due to the excellent $^1O_2$ generation ability and catalytic activity, we explored the anti-cancer potential of BSA@Au on 4T1 tumor-bearing mice. Firstly, we evaluated the hypoxia modulation performance of BSA@Au. After i.v. injection of BSA@Au, the obtained immunofluorescence images of tumor sections showed that the hypoxic areas of tumor tissue markedly decreased from ~46.2% to ~28.2% (Figure 5A,B). This revealed that BSA@Au had desirable catalase-like activity to decompose the overexpressed H_2O_2 within the tumor region to produce O_2 for alleviating the hypoxic tumor microenvironment.

Subsequently, we investigated the in vivo PDT outcomes of BSA@Au. Mice bearing 4T1 tumor were divided into four groups with random (n = 5): (1) Control; (2) Laser; (3) BSA@Au; (4) BSA@Au + Laser. For group (4), 10 h after i.v. injection of BSA@Au, the mice were irradiated by 808 nm laser (0.3 W/cm^2, 30 min). Notably, all mice from groups (2)–(4) only received a single-dose injection and/or single-dose laser irradiation during treatment. Moreover, we monitored the temperature changes of irradiated regions during the treatment. No obvious thermal increase was observed (Figure S8), which suggested that only the PDT effect (without photothermal effect) was involved in the killing of cancer cells. The tumor volume variation and body weights were recorded every 2 days. Results showed that the tumor growth was significantly inhibited in the group (4) whereas the tumor volumes increased quickly in groups (1)–(3), indicating the superior antitumor efficiency of BSA@Au in combination with laser irradiation (Figures 6C and S9). Based on the efficient anti-cancer ability, mice from BSA@Au + Laser group survived for a much longer period (60 days) compared with the other three groups (Figure 5D).

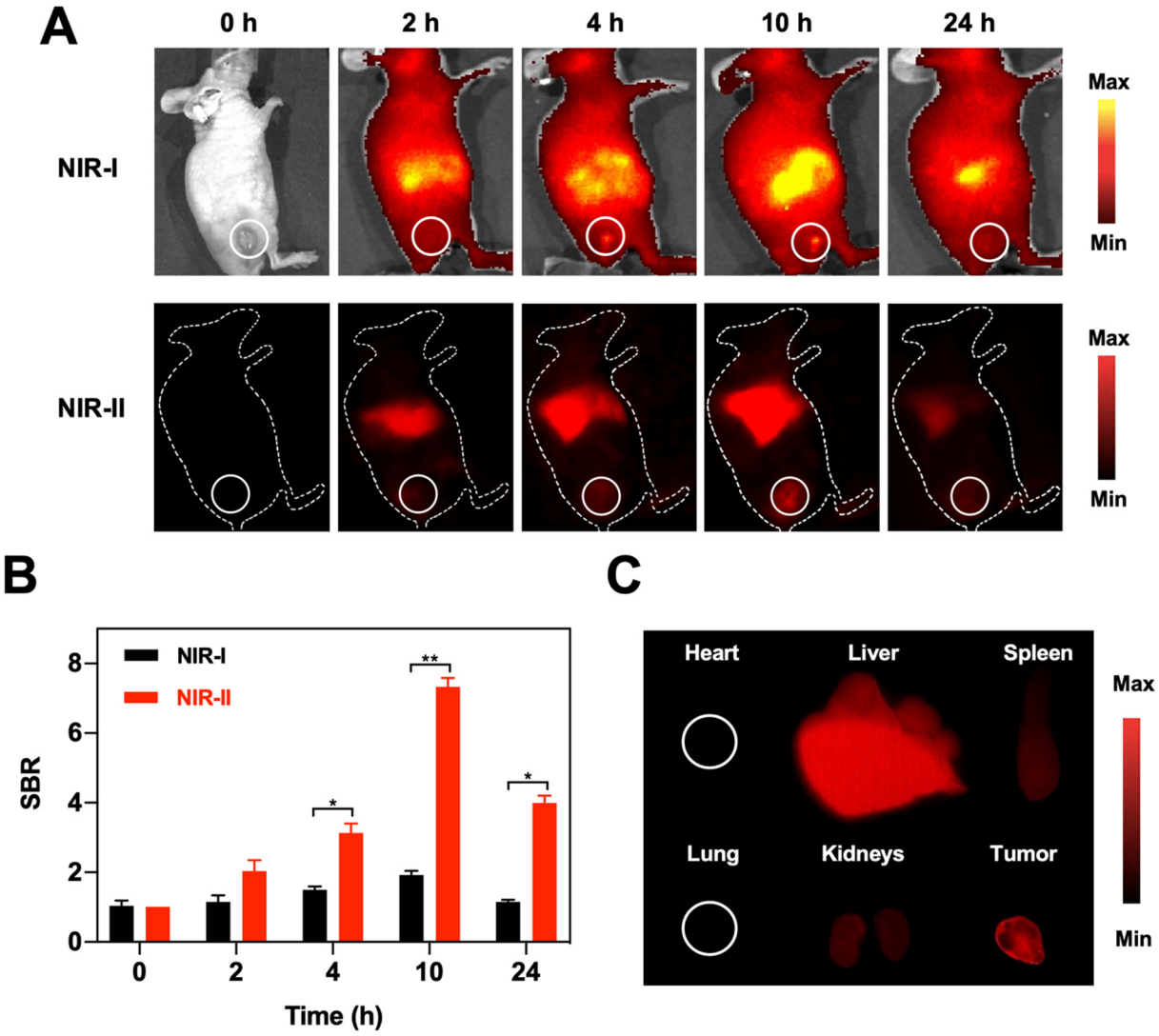

Figure 4. NIR-I and NIR-II FL imaging. (**A**) NIR-I and NIR-II FL images of 4T1 tumor-bearing mice at different time points (0, 2, 4, 10, and 24 h) post i.v. injection of BSA@Au. (**B**) SBR comparison between in vivo NIR-I FL and NIR-II FL images of 4T1 tumor-bearing mice. (**C**) The NIR-II FL images of main organs (heart, liver, spleen, lung, and kidneys) and tumor harvested from 4T1 tumor-bearing mice at 10 h post i.v. injection of BSA@Au. * $p < 0.05$, ** $p < 0.01$.

Meanwhile, tumor tissues from all groups were collected on the next day after various treatments for H&E staining and TUNEL assay. Obvious cell apoptosis and necrosis were found in BSA@Au + Laser group; in contrast, nearly no abnormality was detected in Control, Laser, and BSA@Au groups (Figure 5E). These results further showed that single-dose BSA@Au injection combined with single laser irradiation possessed great damage to cancer tissues. In addition, during the whole therapy process, no body fluctuation was recorded (Figure S10), indicating the high biosafety of BSA@Au combined with laser for PDT. The results together demonstrated that BSA@Au could remarkably modulate hypoxia and realize efficient in vivo anti-tumor outcomes under NIR-II FL imaging guidance.

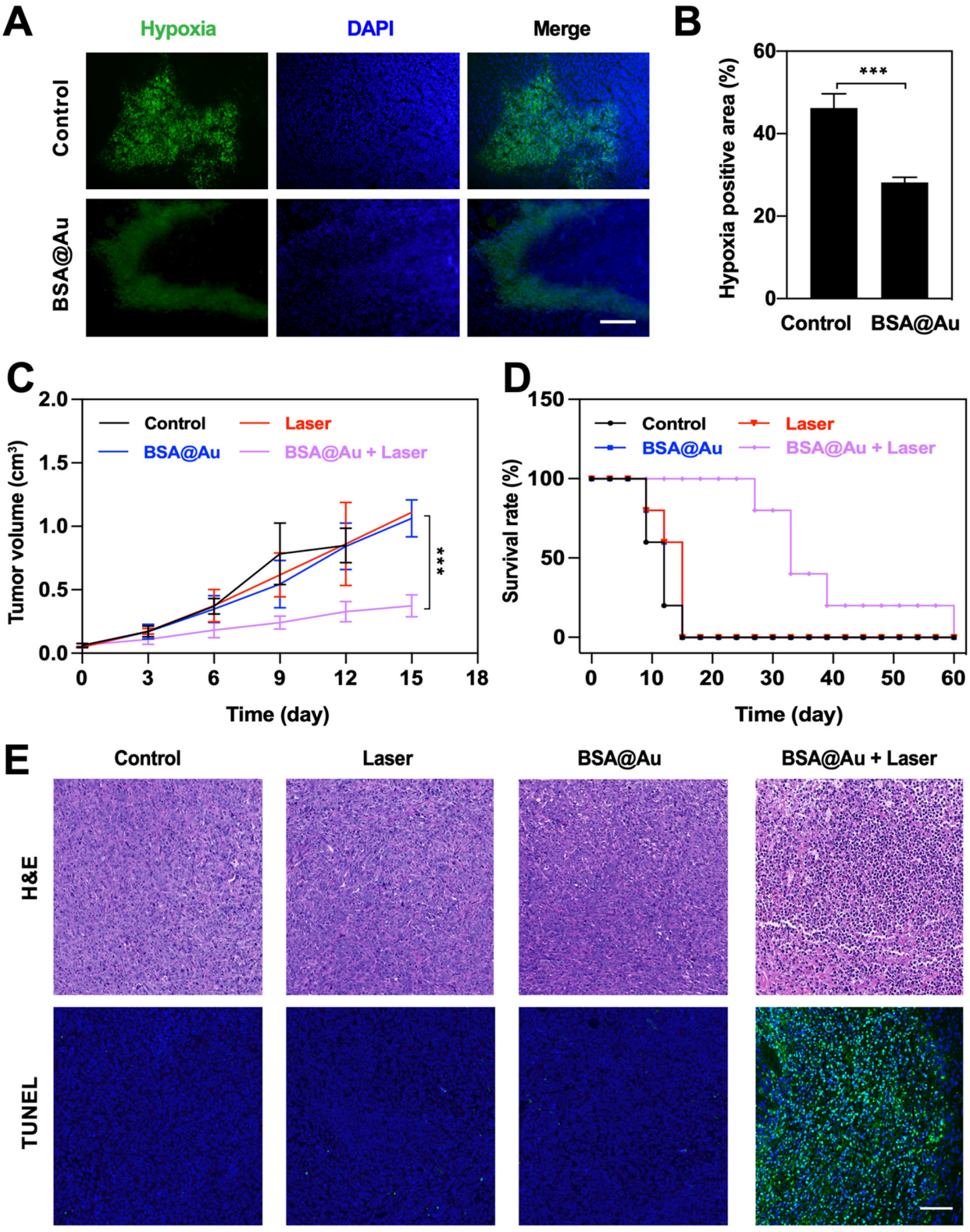

Figure 5. In vivo anti-tumor effect. (**A**) Representative immunofluorescence images of positive hypoxia area of tumor tissues after i.v. injection of PBS or BSA@Au. The scale bar was 100 μm. (**B**) The semi-quantification of positive hypoxia area shown in (**A**). (**C**) Tumor volumes variations over time after different treatments. (**D**) Survival rate of mice received different treatments. (**E**) H&E and TUNEL assay of tumor tissue sections from mice received different treatments. The scale bar was 100 μm. *** $p < 0.005$.

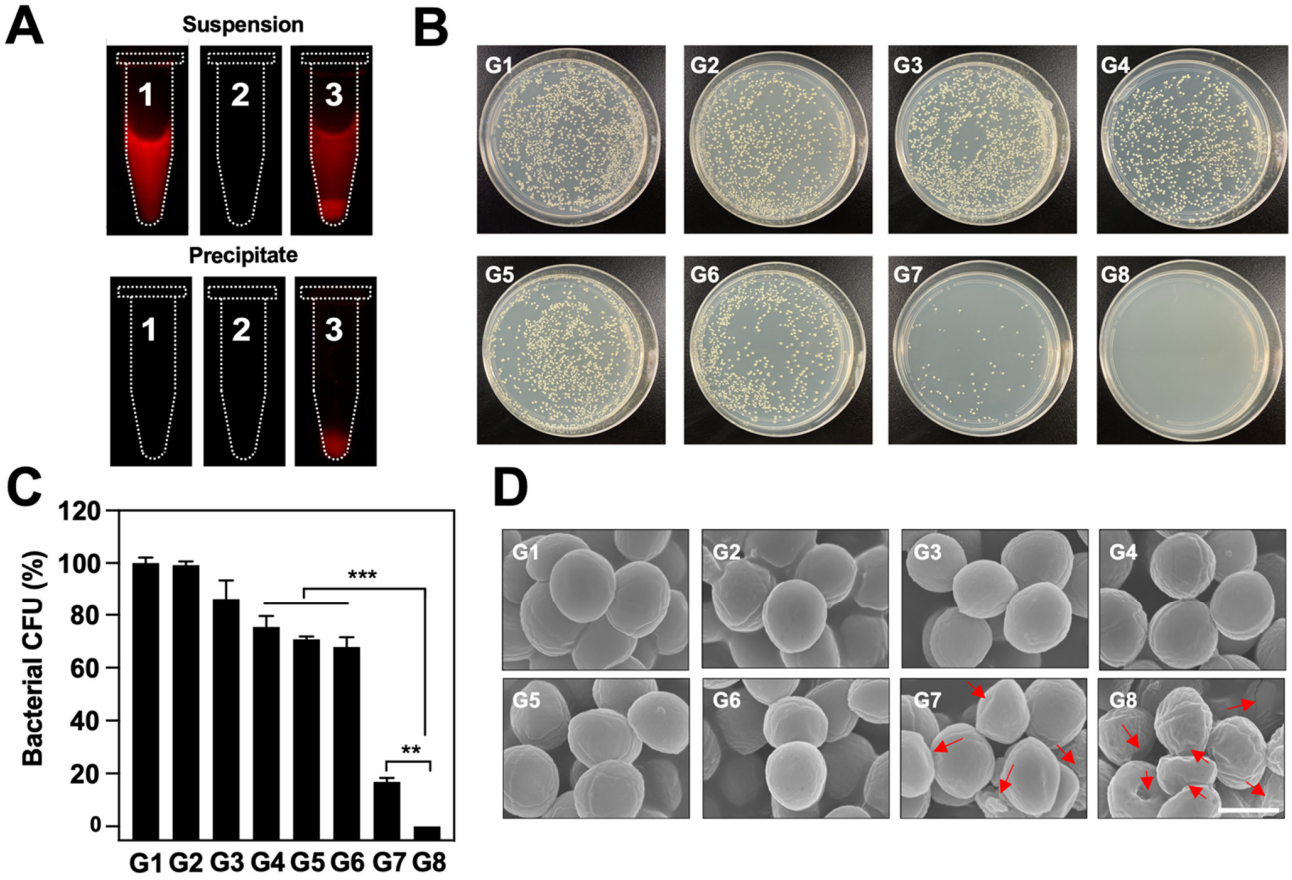

Figure 6. The anti-bacterial efficacy of BSA@Au. (**A**) Observation of BSA@Au binding with MRSA by NIR-II FL imaging. Tube 1, 2, and 3 contained the BSA@Au solution, MRSA solution, and the mixed suspension of BSA@Au and MRSA, respectively. (**B**) MRSA bacterial colonies test on LB agar plates after different treatments. (**C**) Quantification of survival rate of MRSA cells after different treatments. (**D**) Representative SEM images of MRSA exposed to different treatments. The red arrow indicates the crimple, hollow, and crack of MRSA. The scale bar was 1 μm. In (**C**,**D**), G1: PBS; G2: Laser; G3: BSA@Au; G4: H_2O_2; G5: BSA@Au + H_2O_2; G6: H_2O_2 + Laser; G7: BSA@Au + Laser; G8: BSA@Au + H_2O_2 + Laser. ** $p < 0.01$, *** $p < 0.005$.

3.6. In Vitro Antibacterial Efficacy

Bacterial infection have been considered as a key element of cancer management [42]. Given that the infection microenvironment is similar to tumor microenvionment, which features low O_2 and high expression of H_2O_2 [39,40,43], we investigated the anti-bacterial capability of BSA@Au by boosted PDT effect. MRSA, a known type of drug-resistant bacterium, was involved for further evaluation. Inspired by previous reports that human serum albumin has a unique affinity with MRSA [44], we investigated the binding capability of the BSA@Au towards MRSA. Tube 1 was set as the control group, only containing BSA@Au solution; in tubes 2 and 3, MRSA was incubated with PBS or BSA@Au for 4 h, respectively. The three samples were imaged under the NIR-II FL imaging system after centrifugation (5000 rpm, 5 min). The intense signal in tube 3 displayed that BSA@Au could tightly bind with MRSA. Notably, the FL signal of the suspensions was from free BSA@Au solutions, and the FL signal of the precipitates was from the BSA@Au binding with MRSA because BSA@Au could not be spun down at a low centrifugation speed unless they were bound with MRSA (Figure 6A). Then, we evaluated the in vitro anti-bacterial efficacy of BSA@Au in combination with 808 nm laser irradiation. MRSA suspensions were divided into eight groups: (1) Control; (2) Laser; (3) BSA@Au; (4) H_2O_2; (5) H_2O_2 + Laser; (6) BSA@Au + H_2O_2; (7) BSA@Au + Laser; and (8) BSA@Au + H_2O_2 + Laser. Compared with

other treatments, the group (7) killing~70% of the bacteria because of the good toxic $^1O_2$ generation ability of BSA@Au (Figure 6B, C). Considering the hypoxic microenvironment within infectious tissues, which lacks O_2 and overexpresses H_2O_2, we added H_2O_2 (200 μM) to simulate the bacteria-infected microenvironment. Excitingly, no live bacteria colonies (~0%) was observed in group (8), revealing enhanced antibacterial effect after O_2 enrichment within infectious microenvironment. More visibly, as shown in the SEM images, the MRSA cells remained intact with grape-like morphology in groups (1)–(6). However, the MRSA bacteria were distorted and denatured in group (7)–(8). Moreover, the obvious shrinking and cracking of bacteria in group (8) were recorded (Figure 6D) due to $^1O_2$ generated from BSA@Au and H_2O_2 under 808 nm laser irradiation.

3.7. In Vivo Antibacterial Efficacy

To further verify the in vivo anti-bacterial effect, we established a MRSA-infected wound model on Balb/C mice, and then recorded the wound closure and bacterial residue after different treatments. At first, we observed the in vivo NIR-II FL imaging of MRSA-infected wound by local injection of BSA@Au. The bright FL signal was collected, and the SBR was determined to be about 66.8 (Figure S11), demonstrating the potential of BSA@Au as an NIR-II FL probe for in vivo imaging. The wounds treated by BSA@Au + Laser showed a significantly faster healing speed than those of the group (1)–(3), and almost completely healed within 12 days, whereas the wound areas of control group were still about 85.5% of the original wounds (Figure 7A,B). In addition, at the end of the treatment period, we collected the wound tissues from healthy mouse, control group, and BSA@Au + Laser group for continuing cultivation in LB culture medium. As expected, a large number of live MRSA cells were observed in the control group, whereas no bacteria remained in the healthy mouse and BSA@Au + Laser groups because of the excellent anti-bacterial effect of the treatment (Figure 7C). The skin tissues were also used for histology analysis. H&E staining assay displayed that obvious effusion, loose dermis, and inflammatory cells were found in the infected tissue, whereas less necrosis, fewer granulated cells, and more fibrous tissues were observed in the cured wound (Figure 7D). During the whole treatment, no obvious changes in body weight were observed, suggesting PDT for MRSA therapy was safe and biocompatible (Figure S12). Moreover, during the PDT process, the skin temperature did not increase (Figure S13), which excluded the photothermal effect. MRSA-infection as a drug-resistant infectious disease showed little response to clinical antibiotics. However, PDT, as a novel treatment strategy for bacterial infections, could achieve the superb anti-MRSA effect and avoid treatment resistance without using antibiotics. Hence, in the future, BSA@Au might be utilized to detect and treat the deep-seated infections in NIR-II phototheranostic platform.

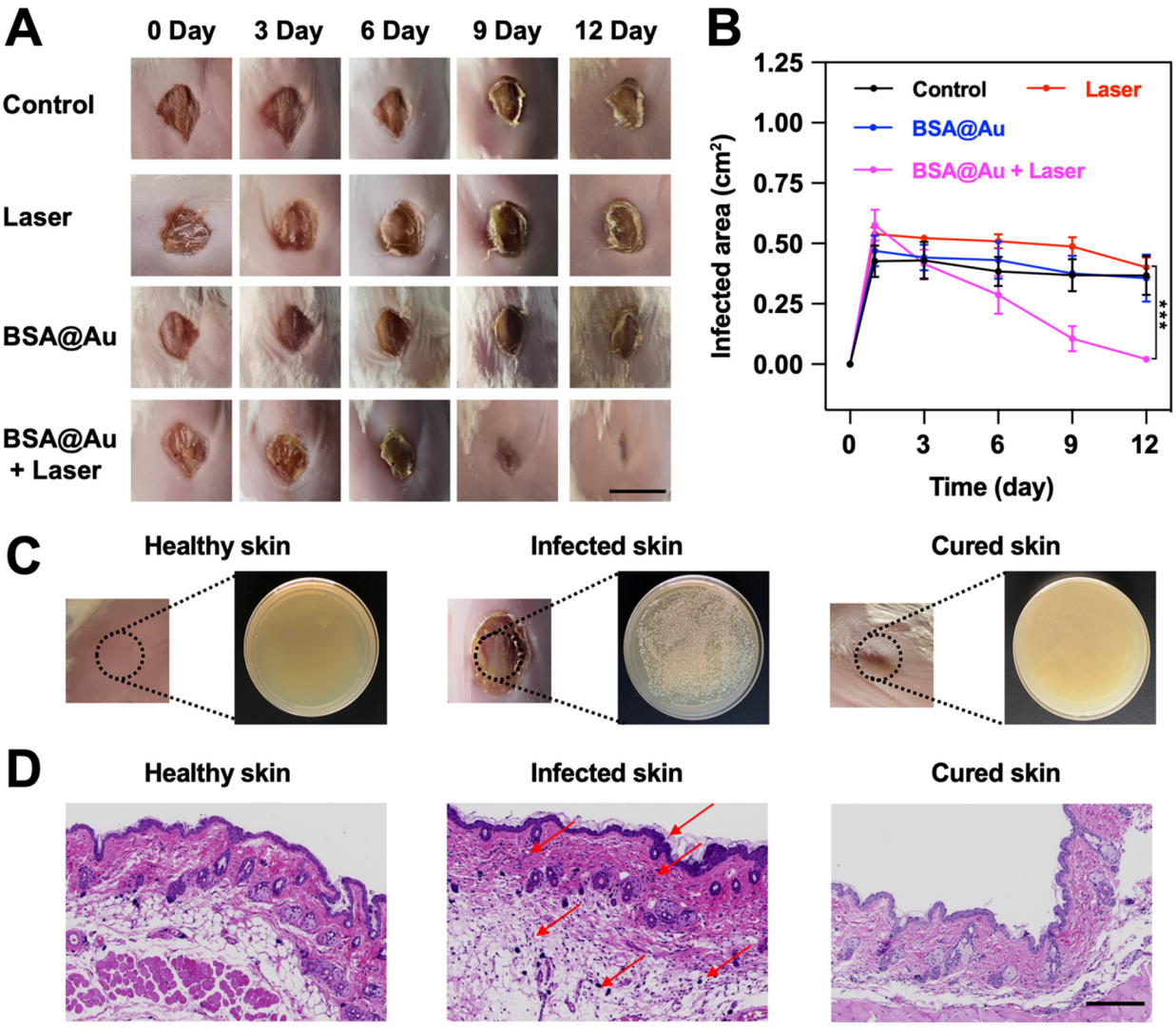

Figure 7. In vivo anti-bacterial effect. (**A**) Photographs of the infectious wounds after in vivo treatments. The scale bar was 1 cm. (**B**) Quantitative analysis of wound areas over time. (**C**) The MRSA colonies on LB-agar plates from the healthy skin tissue, the infected skin tissue, and the cured skin tissue, respectively. (**D**) H&E staining analysis of wounds from the healthy skin tissue, the infected skin tissue, and the cured skin tissue, respectively. The scale bar was 200 μm, and the red arrows represented tissue inflammation. *** $p < 0.005$.

4. Conclusions

In summary, we provided proof-of-principle evidence for the application of an O_2 self-sufficient photosensitizer for boosted cancer/infection PDT under the guidance of NIR-II FL imaging. In this system, BSA@Au was endowed with strong NIR-II FL emission, superb fluorescent QY (~3.5%), strong photobleaching resistance, excellent catalase-like activity, as well as good biocompatibility to realize imaging-guided PDT for cancer and bacteria-infected lesions. With bright NIR-II imaging performance, BSA@Au visualized the tumor location with high SBR (~7.3) and biodistribution, as well as the metabolism pathway itself, enabling high-performance imaging guided PDT. Moreover, BSA@Au served as a catalase mimic decomposing H_2O_2 to O_2 for alleviating a hypoxic microenvironment to augment O_2-dependent PDT. With single 808 nm laser irradiation, it achieved efficient tumor growth inhibition and MRSA-infection curation. Therefore, the developed BSA@Au might fulfill the unmet need for phototheranostics of cancer and bacterial infections.

Supplementary Materials: The following supporting information can be downloaded at: https://www.mdpi.com/article/10.3390/pharmaceutics14081645/s1, Table S1: The preparation optimization of BSA@Au; Table S2: Comparison of kinetic parameters among nanozymes; Table S3: Blood sample examination of mice; Figure S1: Optimization of BSA@Au; Figure S2: Fluorescent QY of BSA@Au; Figure S3: Penetration depth of NIR-I and NIR-II FL imaging; Figure S4: Photostability of BSA@Au; Figure S5: Catalase-like activity of BSA@Au; Figure S6: Biosafety of BSA@Au; Figure S7: Ex vivo FL images; Figure S8: Temperature of mice during cancer PDT; Figure S9: Tumor inhibition of mice received different treatments; Figure S10: Body weights of mice during cancer PDT; Figure S11: In vivo NIR-II FL imaging for MRSA-infected mice; Figure S12: Body weights of mice during MRSA PDT; Figure S13: Temperature of mice during MRSA PDT. References [45–52] are cited in the Supplementary Materials.

Author Contributions: Conceptualization, Z.S. and Y.L.; data curation, D.H.; formal analysis, Q.D.; funding acquisition, H.M., W.L., L.Z., Z.S. and Y.L.; investigation, Z.Y.; methodology, Q.D., S.Z. and N.S.; project administration, Z.S. and Y.L.; resources, Z.Y., Z.S. and Y.L.; software, Q.D.; supervision, Z.S. and Y.L.; validation, S.Z., N.S. and Y.L.; visualization, Q.D.; writing—original draft, Q.D.; writing—review & editing, Z.S. and Y.L. All authors have read and agreed to the published version of the manuscript.

Funding: This work is supported by the Natural Science Foundation of China (92159304, 82102081, 82171958, 81901812, 81971638, 82027803, 81927807, 82071949, 81871371, 81801720, 81701711, 81671709, 81827807), Science and Technology Planning Project of Guangzhou City (201804010106), and President Foundation of Nanfang Hospital, Southern Medical University (2020A001), CAS Key Laboratory of Health Informatics (2011DP173015), the Science and Technology Key Project of Shenzhen (JCYJ20190812163614809, JCYJ20200109114612308, JCYJ20210324120011030), Guangdong Basic and Applied Basic Research Fund (2020A1515110011, 2020A1515010395, 2022A1515010384), Key Laboratory for Magnetic Resonance and Multimodality Imaging of Guangdong Province (2020B1212060051), and the Key Technology and Equipment R&D Program of Major Science and Technology Infrastructure of Shenzhen (202100102, 202100104).

Institutional Review Board Statement: The animal study protocol was approved by the Institutional Animal Care and Use of Shenzhen Institutes of Advanced Technology (protocol code: SIAT-IACUC-20190304-YGS-YXZX-SZH-01, and date of approval: 20190304).

Informed Consent Statement: Not applicable.

Data Availability Statement: Data supporting reported results beyond what is reported in this manuscript are available upon reasonable request from the corresponding authors.

Acknowledgments: The authors appreciate the contribution of Zihan Mei (Shanghai Ruijin Hospital) to provide the method to establish MRSA-infected mouse model.

Conflicts of Interest: The authors declare no conflict of interest.

References

1. Hong, G.; Antaris, A.L.; Dai, H. Near-Infrared Fluorophores for Biomedical Imaging. *Nat. Biomed. Eng.* **2017**, *1*, 10. [CrossRef]
2. Zhu, S.; Tian, R.; Antaris, A.L.; Chen, X.; Dai, H. Near-Infrared-II Molecular Dyes for Cancer Imaging and Surgery. *Adv. Mater.* **2019**, *31*, 1900321. [CrossRef] [PubMed]
3. Lin, H.; Lin, Z.; Zheng, K.; Wang, C.; Lin, L.; Chen, J.; Song, J. Near-Infrared-II Nanomaterials for Fluorescence Imaging and Photodynamic Therapy. *Adv. Opti. Mater.* **2021**, *9*, 2002177. [CrossRef]
4. Dai, H.; Shen, Q.; Shao, J.; Wang, W.; Gao, F.; Dong, X. Small Molecular NIR-II Fluorophores for Cancer Phototheranostics. *Innovation* **2021**, *2*, 100082. [CrossRef] [PubMed]
5. Turan, I.S.; Yildiz, D.; Turksoy, A.; Gunaydin, G.; Akkaya, E.U. A Bifunctional Photosensitizer for Enhanced Fractional Photodynamic Therapy: Singlet Oxygen Generation in the Presence and Absence of Light. *Angew. Chem.* **2016**, *128*, 2925–2928. [CrossRef]
6. Zheng, Z.; Zhang, T.; Liu, H.; Chen, Y.; Kwok, R.T.K.; Ma, C.; Zhang, P.; Sung, H.H.Y.; Williams, I.D.; Lam, J.W.Y.; et al. Bright Near-Infrared Aggregation-Induced Emission Luminogens with Strong Two-Photon Absorption, Excellent Organelle Specificity, and Efficient Photodynamic Therapy Potential. *ACS Nano* **2018**, *12*, 8145–8159. [CrossRef]
7. Thomas, A.P.; Palanikumar, L.; Jeena, M.T.; Kim, K.; Ryu, J.-H. Cancer-Mitochondria-Targeted Photodynamic Therapy with Supramolecular Assembly of HA and a Water Soluble NIR Cyanine Dye. *Chem. Sci.* **2017**, *8*, 8351–8356. [CrossRef]

8. Schmitt, J.; Heitz, V.; Sour, A.; Bolze, F.; Ftouni, H.; Nicoud, J.; Flamigni, L.; Ventura, B. Diketopyrrolopyrrole-Porphyrin Conjugates with High Two-Photon Absorption and Singlet Oxygen Generation for Two-Photon Photodynamic Therapy. *Angew. Chem. Int. Ed.* **2015**, *54*, 169–173. [CrossRef]
9. Ge, J.; Lan, M.; Zhou, B.; Liu, W.; Guo, L.; Wang, H.; Jia, Q.; Niu, G.; Huang, X.; Zhou, H.; et al. A Graphene Quantum Dot Photodynamic Therapy Agent with High Singlet Oxygen Generation. *Nat. Commun.* **2014**, *5*, 4596. [CrossRef]
10. Mou, J.; Lin, T.; Huang, F.; Chen, H.; Shi, J. Black Titania-Based Theranostic Nanoplatform for Single NIR Laser Induced Dual-Modal Imaging-Guided PTT/PDT. *Biomaterials* **2016**, *84*, 13–24. [CrossRef]
11. Wang, H.; Yang, X.; Shao, W.; Chen, S.; Xie, J.; Zhang, X.; Wang, J.; Xie, Y. Ultrathin Black Phosphorus Nanosheets for Efficient Singlet Oxygen Generation. *J. Am. Chem. Soc.* **2015**, *137*, 11376–11382. [CrossRef] [PubMed]
12. Feng, G.; Fang, Y.; Liu, J.; Geng, J.; Ding, D.; Liu, B. Multifunctional Conjugated Polymer Nanoparticles for Image-Guided Photodynamic and Photothermal Therapy. *Small* **2017**, *13*, 1602807. [CrossRef] [PubMed]
13. Han, H.-H.; Wang, C.-Z.; Zang, Y.; Li, J.; James, T.D.; He, X.-P. Supramolecular Core-Glycoshell Polythiophene Nanodots for Targeted Imaging and Photodynamic Therapy. *Chem. Commun.* **2017**, *53*, 9793–9796. [CrossRef] [PubMed]
14. Vankayala, R.; Huang, Y.-K.; Kalluru, P.; Chiang, C.-S.; Hwang, K.C. First Demonstration of Gold Nanorods-Mediated Photodynamic Therapeutic Destruction of Tumors via Near Infra-Red Light Activation. *Small* **2014**, *10*, 1612–1622. [CrossRef]
15. Huang, H.; Yu, B.; Zhang, P.; Huang, J.; Chen, Y.; Gasser, G.; Ji, L.; Chao, H. Highly Charged Ruthenium (II) Polypyridyl Complexes as Lysosome-Localized Photosensitizers for Two-Photon Photodynamic Therapy. *Angew. Chem. Int. Ed.* **2015**, *54*, 14049–14052. [CrossRef]
16. Zhao, J.; Zhong, D.; Zhou, S. NIR-I-to-NIR-II Fluorescent Nanomaterials for Biomedical Imaging and Cancer Therapy. *J. Mater. Chem. B* **2018**, *6*, 349–365. [CrossRef]
17. Zhang, Z.; Xu, W.; Kang, M.; Wen, H.; Guo, H.; Zhang, P.; Xi, L.; Li, K.; Wang, L.; Wang, D.; et al. An All-Round Athlete on the Track of Phototheranostics: Subtly Regulating the Balance between Radiative and Nonradiative Decays for Multimodal Imaging-Guided Synergistic Therapy. *Adv. Mater.* **2020**, *32*, 2003210. [CrossRef]
18. Tang, C.; Song, C.; Wei, Z.; Liang, C.; Ran, J.; Cai, Y.; Dong, X.; Han, W. Polycyclic Naphthalenediimide-Based Nanoparticles for NIR-II Fluorescence Imaging Guided Phototherapy. *Sci. China Chem.* **2020**, *63*, 946–956. [CrossRef]
19. Bian, H.; Ma, D.; Zhang, X.; Xin, K.; Yang, Y.; Peng, X.; Xiao, Y. Tailored Engineering of Novel Xanthonium Polymethine Dyes for Synergetic PDT and PTT Triggered by 1064 nm Laser toward Deep-Seated Tumors. *Small* **2021**, *17*, 2100398. [CrossRef]
20. Jin, R. Quantum Sized, Thiolate-Protected Gold Nanoclusters. *Nanoscale* **2010**, *2*, 343–362. [CrossRef]
21. Song, X.; Zhu, W.; Ge, X.; Li, R.; Li, S.; Chen, X.; Song, J.; Xie, J.; Chen, X.; Yang, H. A New Class of NIR-II Gold Nanocluster-Based Protein Biolabels for in vivo Tumor-Targeted Imaging. *Angew. Chem. Int. Ed.* **2021**, *60*, 1306–1312. [CrossRef] [PubMed]
22. Liu, H.; Hong, G.; Luo, Z.; Chen, J.; Chang, J.; Gong, M.; He, H.; Yang, J.; Yuan, X.; Li, L.; et al. Atomic-Precision Gold Clusters for NIR-II Imaging. *Adv. Mater.* **2019**, *31*, 1901015. [CrossRef] [PubMed]
23. Li, D.; Liu, Q.; Qi, Q.; Shi, H.; Hsu, E.; Chen, W.; Yuan, W.; Wu, Y.; Lin, S.; Zeng, Y.; et al. Gold Nanoclusters for NIR-II Fluorescence Imaging of Bones. *Small* **2020**, *16*, 2003851. [CrossRef]
24. Yang, Y.; Yu, Y.; Chen, H.; Meng, X.; Ma, W.; Yu, M.; Li, Z.; Li, C.; Liu, H.; Zhang, X.; et al. Illuminating Platinum Transportation While Maximizing Therapeutic Efficacy by Gold Nanoclusters via Simultaneous Near-Infrared-I/II Imaging and Glutathione Scavenging. *ACS Nano* **2020**, *14*, 13536–13547. [CrossRef] [PubMed]
25. Wang, W.; Kong, Y.; Jiang, J.; Xie, Q.; Huang, Y.; Li, G.; Wu, D.; Zheng, H.; Gao, M.; Xu, S.; et al. Engineering the Protein Corona Structure on Gold Nanoclusters Enables Red-Shifted Emissions in the Second Near-infrared Window for Gastrointestinal Imaging. *Angew. Chem. Int. Ed.* **2020**, *59*, 22431–22435. [CrossRef] [PubMed]
26. Lillo, C.R.; Calienni, M.N.; Rivas Aiello, B.; Prieto, M.J.; Rodriguez Sartori, D.; Tuninetti, J.; Toledo, P.; del Valle Alonso, S.; Moya, S.; Gonzalez, M.C.; et al. BSA-Capped Gold Nanoclusters as Potential Theragnostic for Skin Diseases: Photoactivation, Skin Penetration, in Vitro, and in vivo Toxicity. *Mat. Sci. Eng. C* **2020**, *112*, 110891. [CrossRef]
27. Dan, Q.; Hu, D.; Ge, Y.; Zhang, S.; Li, S.; Gao, D.; Luo, W.; Ma, T.; Liu, X.; Zheng, H.; et al. Ultrasmall Theranostic Nanozymes to Modulate Tumor Hypoxia for Augmenting Photodynamic Therapy and Radiotherapy. *Biomater. Sci.* **2020**, *8*, 973–987. [CrossRef]
28. Xie, J.; Zheng, Y.; Ying, J.Y. Protein-Directed Synthesis of Highly Fluorescent Gold Nanoclusters. *J. Am. Chem. Soc.* **2009**, *131*, 888–889. [CrossRef]
29. Du, B.; Yu, M.; Zheng, J. Transport and Interactions of Nanoparticles in the Kidneys. *Nat. Rev. Mater.* **2018**, *3*, 358–374. [CrossRef]
30. Loynachan, C.N.; Soleimany, A.P.; Dudani, J.S.; Lin, Y.; Najer, A.; Bekdemir, A.; Chen, Q.; Bhatia, S.N.; Stevens, M.M. Renal Clearable Catalytic Gold Nanoclusters for in vivo Disease Monitoring. *Nat. Nanotechnol.* **2019**, *14*, 883–890. [CrossRef]
31. Chen, D.; Li, J. Ultrasmall Au Nanoclusters for Bioanalytical and Biomedical Applications: The Undisclosed and Neglected Roles of Ligands in Determining the Nanoclusters' Catalytic Activities. *Nanoscale Horiz.* **2020**, *5*, 1355–1367. [CrossRef] [PubMed]
32. Shang, Y.; Min, C.; Hu, J.; Wang, T.; Liu, H.; Hu, Y. Synthesis of Gold Nanoparticles by Reduction of $HAuCl_4$ under UV Irradiation. *Solid State Sci.* **2013**, *15*, 17–23. [CrossRef]
33. Lin, C.; Tao, K.; Hua, D.; Ma, Z.; Zhou, S. Size Effect of Gold Nanoparticles in Catalytic Reduction of P-Nitrophenol with $NaBH_4$. *Molecules* **2013**, *18*, 12609–12620. [CrossRef] [PubMed]
34. Zhu, M.; Aikens, C.M.; Hollander, F.J.; Schatz, G.C.; Jin, R. Correlating the Crystal Structure of a Thiol-Protected Au_{25} Cluster and Optical Properties. *J. Am. Chem. Soc.* **2008**, *130*, 5883–5885. [CrossRef]

35. Poderys, V.; Jarockyte, G.; Bagdonas, S.; Karabanovas, V.; Rotomskis, R. Protein-Stabilized Gold Nanoclusters for PDT: ROS and Singlet Oxygen Generation. *J. Photochem. Photobiol. B Biol. B* **2020**, *204*, 111802. [CrossRef]
36. Pang, Z.; Li, Q.; Jia, Y.; Yan, W.; Qi, J.; Guo, Y.; Hu, F.; Zhou, D.; Jiang, X. Controlling the Pyridinium-Zwitterionic Ligand Ratio on Atomically Precise Gold Nanoclusters Allowing for Eradicating Gram-Positive Drug-Resistant Bacteria and Retaining Biocompatibility. *Chem. Sci.* **2021**, *12*, 14871–14882. [CrossRef]
37. Li, S.; Ma, Q.; Wang, C.; Yang, K.; Hong, Z.; Chen, Q.; Song, J.; Song, X.; Yang, H. Near-Infrared II Gold Nanocluster Assemblies with Improved Luminescence and Biofate for In Vivo Ratiometric Imaging of H_2S. *Anal. Chem.* **2022**, *94*, 2641–2647. [CrossRef]
38. Kong, Y.; Santos-Carballal, D.; Martin, D.; Sergeeva, N.N.; Wang, W.; Liu, G.; Johnson, B.; Bhayana, B.; Lin, Z.; Wang, Y.; et al. A NIR-II-Emitting Gold Nanocluster-Based Drug Delivery System for Smartphone-Triggered Photodynamic Theranostics with Rapid Body Clearance. *Mater. Today* **2021**, *51*, 96–107. [CrossRef]
39. Hockel, M.; Vaupel, P. Tumor Hypoxia: Definitions and Current Clinical, Biologic, and Molecular Aspects. *JNCI J. Natl. Cancer Inst.* **2001**, *93*, 266–276. [CrossRef]
40. Devraj, G.; Beerlage, C.; Brüne, B.; Kempf, V.A.J. Hypoxia and HIF-1 Activation in Bacterial Infections. *Microbes Infect.* **2017**, *19*, 144–156. [CrossRef]
41. Johnson, K.A.; Goody, R.S. The Original Michaelis Constant: Translation of the 1913 Michaelis–Menten Paper. *Biochemistry* **2011**, *50*, 8264–8269. [CrossRef] [PubMed]
42. Elsland, D.; Neefjes, J. Bacterial Infections and Cancer. *EMBO Rep.* **2018**, *19*. [CrossRef] [PubMed]
43. Schaffer, K.; Taylor, C.T. The Impact of Hypoxia on Bacterial Infection. *FEBS J.* **2015**, *282*, 2260–2266. [CrossRef] [PubMed]
44. Chan, P.-H.; Chen, Y.-C. Human Serum Albumin Stabilized Gold Nanoclusters as Selective Luminescent Probes for Staphylococcus Aureus and Methicillin-Resistant Staphylococcus Aureus. *Anal. Chem.* **2012**, *84*, 8952–8956. [CrossRef]
45. Murphy, J.E.; Beard, M.C.; Norman, A.G.; Ahrenkiel, S.P.; Johnson, J.C.; Yu, P.; Mićić, O.I.; Ellingson, R.J.; Nozik, A.J. PbTe Colloidal Nanocrystals: Synthesis, Characterization, and Multiple Exciton Generation. *J. Am. Chem. Soc.* **2006**, *128*, 3241–3247. [CrossRef]
46. Wang, Q.; Xu, J.; Geng, R.; Cai, J.; Li, J.; Xie, C.; Tang, W.; Shen, Q.; Huang, W.; Fan, Q. High Performance One-for-All Phototheranostics: NIR-II Fluorescence Imaging Guided Mitochondria-Targeting Phototherapy with a Single-Dose Injection and 808 nm Laser Irradiation. *Biomaterials* **2020**, *231*, 119671. [CrossRef]
47. Mu, J.; Zhang, L.; Zhao, M.; Wang, Y. Catalase Mimic Property of Co_3O_4 Nanomaterials with Different Morphology and Its Application as a Calcium Sensor. *ACS Appl. Mater. Interfaces* **2014**, *6*, 7090–7098. [CrossRef]
48. Fan, J.; Yin, J.-J.; Ning, B.; Wu, X.; Hu, Y.; Ferrari, M.; Anderson, G.J.; Wei, J.; Zhao, Y.; Nie, G. Direct Evidence for Catalase and Peroxidase Activities of Ferritin–Platinum Nanoparticles. *Biomaterials* **2011**, *32*, 1611–1618. [CrossRef]
49. Wang, X.; Zhang, Y.; Li, T.; Tian, W.; Zhang, Q.; Cheng, Y. Generation 9 Polyamidoamine Dendrimer Encapsulated Platinum Nanoparticle Mimics Catalase Size, Shape, and Catalytic Activity. *Langmuir* **2013**, *29*, 5262–5270. [CrossRef]
50. Deng, H.; Shen, W.; Peng, Y.; Chen, X.; Yi, G.; Gao, Z. Nanoparticulate Peroxidase/Catalase Mimetic and Its Application. *Chem. Eur. J.* **2012**, *18*, 8906–8911. [CrossRef]
51. Su, H.; Liu, D.-D.; Zhao, M.; Hu, W.-L.; Xue, S.-S.; Cao, Q.; Le, X.-Y.; Ji, L.-N.; Mao, Z.-W. Dual-Enzyme Characteristics of Polyvinylpyrrolidone-Capped Iridium Nanoparticles and Their Cellular Protective Effect against H_2O_2-Induced Oxidative Damage. *ACS Appl. Mater. Interfaces* **2015**, *7*, 8233–8242. [CrossRef] [PubMed]
52. Liu, C.-P.; Wu, T.-H.; Liu, C.-Y.; Chen, K.-C.; Chen, Y.-X.; Chen, G.-S.; Lin, S.-Y. Self-Supplying O_2 through the Catalase-Like Activity of Gold Nanoclusters for Photodynamic Therapy against Hypoxic Cancer Cells. *Small* **2017**, *13*, 1700278. [CrossRef] [PubMed]